Materials Today Chemistry 24 (2022) 100925

Contents lists available at ScienceDirect

Materials Today Chemistry

journal homepage: www.journals.elsevier.com/materials-today-chemistry/

Morphological and chemical evolution of transient interfaces during zinc oxide cold sintering process

S.H. Bang [a, *], M.Y. Sengul [a, b], Z. Fan [a], A. Ndayishimiye [a], A.C.T. van Duin [a, b], C.A. Randall [a]

[a] Materials Research Institute, The Pennsylvania State University, University Park, PA, 16802, USA
[b] Department of Mechanical Engineering, The Pennsylvania State University, University Park, PA, 16802, USA

ARTICLE INFO

Article history:
Received 9 December 2021
Received in revised form
25 March 2022
Accepted 30 March 2022
Available online 12 May 2022

Keywords:
ReaxFF
Molecular dynamics
Low-temperature sintering
Grain growth
Surface area

ABSTRACT

Although zinc oxide has a high melting point of 1975 °C, the recent development of the cold sintering process has shown that highly dense polycrystalline ceramics can be obtained at 150 °C or below. As such unusual densification does not yet have fully elucidated underlying mechanisms, this study aims to provide a comprehensive investigation of transient morphological and chemical interfaces during isothermal dwell. The chemical "transient" interface involves the formation of a zinc carboxylate complex by reacting the host zinc oxide powder and acetic acid solution, which is later consumed for the recrystallization on the lattice of an adjacent grain with a decomposition of the complex. Hence, the final outcome can be a residual-free zinc oxide phase. Regarding the morphological evolution, gas physisorption studies were conducted to quantify the area of solid−vapor interfaces and the Schlaffer model was used to analyze the activation energy for specific surface area reduction. Moreover, transmission electron micrographs revealed that the recrystallization occurs at the interface between crystalline grain and carbon-rich amorphous phase. After 30 minutes of isothermal dwell, the area of the amorphous phase was significantly decreased while grain size was increased, potentially indicating the recrystallization-induced grain growth and pore closure. The chemical transition at the zinc oxide surface was further investigated using ReaxFF molecular dynamics simulation, observing that acetate molecule acts as a bridging complex to connect zinc ions to the surface. Overall, understanding the evolution of the transient interface is a crucial subject to obtaining a residual-free cold-sintered sample with desired grain size and properties for application developments.

1. Introduction

Sintering is a long historical materials processing method for transforming a natural substance into man-made earthenware that dates back to at least 26,000 years [1]. From then, it has been a well-established bulk and thick film fabrication technique, which is still evolving upon the development of new sintering methods. Although discovering new materials processing can immensely contribute to scientific and technological innovation, the whole investigation may take several decades to understand governing fundamentals and to implement industrial-scale productions. Take spark plasma sintering (SPS), also known as field assisted sintering technique (FAST), as an example, its technological origin was pioneered by Bloxam [2] through developing the first current resistive sintering apparatus in 1906, but it was until the 1990s to have exponentially growing interests in its scientific and industrial implementations for accelerating new materials development [3].

To evaluate the maturity of a particular technology, a concept of Technology Readiness Levels (TRLs) [4] can be regarded as one of the assessment methods to measure a course of developing and utilizing a new sintering methodology where understanding densification kinetics is a crucial step to attain Level 3, which includes analytical predictions. The densification kinetics can be studied by quantifying the shrinkage of a powder compact during a sintering process, but like Kuczynski, a pioneer of theorizing a neck growth model, remarked at the VI International Conference on Sintering in 1985 that the complexity of developing a new model for demonstrating microstructure evolution during sintering process is still far from solved [5]. Especially, in the case of relatively recent non-conventional sintering methods, a densification kinetic study often requires incorporating additional fundamental knowledge to understand related mechanisms. Take the master sintering

* Corresponding author.
E-mail address: sbang@psu.edu (S.H. Bang).

https://doi.org/10.1016/j.mtchem.2022.100925
2468-5194/

curve method [6] as an example, despite its comprehensive applicability [7–9] for estimating sintering activation energy and predicting densification behaviors, a scientific community is still active to find a way to improve the methodological accuracy [10].

Among non-conventional sintering methods, cold sintering process can take a complementary positioning in the powder densification process space for enabling significant energy saving [11] and ceramic matrix polymer composite fabrication [12]. By utilizing uniaxial pressure, transient chemical phase, and homologous temperature below 0.2, the cold sintering has been considered as a non-equilibrium process to develop functional composite materials for various applications [13–15]. Although the term cold sintering may have been widely used to even describe powder compaction behavior or plastic deformation that requires secondary heat treatment to complete the sintering process, its discriminative technological advantages are largely relevant to a single-step low-temperature process. The direct evidence of sintering is observed in the reduction of specific surface area between powder and sintered specimen [16,17] and a high degree of surface area reduction is reported in single-step cold-sintered material systems as well [18–20].

We herein, investigate the densification kinetics based on specific surface area reduction and the evolution of transient morphological and chemical interface during isothermal cold sintering process, where ZnO was used as a model sintering system. We previously reported non-isothermal densification kinetics of ZnO by establishing densification process variables, which are transient chemistry ($\mu(t)$), sintering temperature (T), uniaxial pressure (P) and dwell time (t), and demonstrated its intrinsically low-sintering activation energy during heating [21]. This study is intended to investigate the isothermal densification kinetics and interface evolution using both experimental and computational approaches, which can nurture empirical insights into more comprehensive analytical predictions to be established in due time.

2. Methods

2.1. Cold sintering process

1.0 g of the ZnO powder (Alfa Aesar 40–100 nm APS powder) and 15 wt% of 2 M acetic acid solution were mixed in an agate mortar for 5 minutes. Then, the mixture was transferred into a 13-mm diameter carbon tool steel pressing die (Across International SDS13) with a custom-designed support plate [21] for thermocouple placement shown in Fig. S1 (CAD file available: github.com/sunhwibang/sintering_die). The sintering die was uniaxial pressed under 175 MPa at room temperature for 5 minutes to stabilize the powder compaction where the excessive liquid phase was extruded by the applied pressure. After pre-pressing of the mixture, the pressing die was then heated using a mica band heater where the average heating rate was 15 °C/min. Starting from the initial temperature of 25±1.0 °C, the dwell time was measured from the set isothermal temperature and the steady-state heat fluctuation was within ±5.0 °C. After the set dwell time ranging from 0 to 30 minutes, the uniaxial pressure was released and the pressing die was fan-cooled down to room temperature.

2.2. Materials characterization

The bulk density of a cold-sintered pellet was quantified by dividing the sample weight by the volume:

$$\rho = \frac{m}{\pi r^2 h} \quad (1)$$

where m is the mass of the sample, r is the radius of the sample, and h is the pellet thickness. The diameter was measured by a digital caliper with the accuracy of ±0.01 mm. The thickness was recorded on a pellet surface using a position display unit (Heidenhain ND 280) with the accuracy of ±1 μm. The relative density was then evaluated by taking the bulk density over the theoretical density, which is 5.61 g/cm^3 for ZnO. Brunauer, Emmett, and Teller specific surface area (BET, Micromeritics ASAP 2020) was used to quantify the surface area reduction between powder and the cold sintering process. The degassing condition was N_2 atmosphere for 8 h at 80 °C and such a low-temperature and longtime were chosen to avoid any undesired microstructural changes during the degassing process. Fourier transform infrared spectroscopy (FT-IR, Bruker V70) was done over mid-IR (4000–500 cm^{-1}) to identify functional groups present within a cold-sintered specimen. The fracture surface morphology was analyzed by scanning electron microscope (SEM, FEI NovaSEM 630) and 10-nm iridium sputtering was used to minimize electron charging from the landing energy of 7 keV. A thin specimen was prepared using focus ion beam (FIB, Thermal Scientific Scios 2) for transmission electron microscope (TEM, Telos F200X).

2.3. Computational method

The simulation box used in this study is composed of a condensed and solvent phase: the ZnO region and the liquid region, respectively. The solve phase is composed of acetic acid, water molecules and zinc ions. The surface region was simulated using a ZnO slab in the wurtzite structure, which consists of 7 layers containing 1764 Zn^{2+} and O^{2-} ions. The slab thickness used in the simulations were thicker than the cut-off value of the interatomic interactions. The solvent phase of the simulation box was prepared and equilibrated separately from the condensed phase, and both phases were combined after equilibration. The solvent region is composed of 100 Zn^{2+} ions, 200 acetate molecules (to neutralized the total charge in the chemical system), 300 acetic acid molecules and 500 water molecules. It was experimentally reported that the 2 hydration shells of Zn^{2+} ions are composed of 20 water molecules [22]. The stage of cold sintering, that is of interest in this study, is when the evaporation starts in the system. Therefore, for the sake of accelerating molecular dynamics simulations, we assumed that the solvent phase is slightly saturated and thus, the number of solvent molecules for each ion in the solvent phase was selected as 10. The density of the solvent phase was calculated adjusting the simulation box to keep water density as 1 g/cm^3 and acetic acid density as 1.05 g/cm^3 at the beginning of the simulation.

Once both solvent and condensed phases were equilibrated separately, the solvent region was placed on the top of the ZnO. In order to mimic the experimental conditions in the pore region during cold sintering process, a vacuum region is created in the simulation box on the direction perpendicular to the surface. The vacuum region allows the solve to evaporate, but at the same time, keep the vapor pressure in the system. The ReaxFF interatomic potential used in this study was reoptimized to model ZnO–acetic acid–water chemical systems at elevated temperatures and pressures [23,24], and also in several cold sintering related studies [25]; therefore it is suitable to use in this study. The Amsterdam density function (ADF) software was used in this study [26]. A time step of 0.25 fs combined with velocity–Verlet algorithm was used to calculate the Newtonian equations of motion. The thermostat that is used to keep temperature constant at desired values was selected as a weak Berendsen thermostat [27]. The temperature damping constant was selected as 0.1 ps. All simulations were performed in

NVT ensemble. The simulated boxes were heated slowly to 600 K with an increment of 0.002 K/fs.

3. Results and discussion

3.1. Densification during isothermal sintering

Fig. 1 presents the microstructural evolution between 0 and 30 minutes of isothermal dwell at 150 °C combined with relative density and average grain size measurements. From the series of micrographs, it is evident that the population of small grain diminishes and the grain shape changes from round to faceted, which is likely attributed to grain shape accommodation under the given cold sintering condition. Fig. 2a shows the cumulative frequency of grain size during the given isothermal dwell time. Indeed, the grain size is gradually increasing with respect to the time. While the relative density slightly increases from 94.4% to 97.2%, average grain size significantly increases from 109±47 to 183±41 nm, indicating that grain growth kinetics is dominantly faster than pore closure under these experimental condition based on both grain size and specific surface area measurements. However, the given observation is not entirely consistent with what Nur et al. [28] reported where the degree of grain growth is highly dependent on sintering atmospheres. For the air environment, one of the possible explanations can be closely related to a large difference in sintering temperature ($\Delta T = 100$ °C), which can impact the evolution of transient chemical interfaces. Although the noticeable difference in applied uniaxial pressure ($\Delta P = 130$ MPa) may also affect the grain growth, the pressure-dependent topography study [29] showed that grain size and surface dihedral angle do not have distinguishable morphological changes between 205 and 340 MPa.

The empirical equation relating grain size and time during isothermal dwell was originally proposed by Iida in 1958 [30]:

$$D^n = Kt \tag{2}$$

where D is the average grain size, n is the reciprocal of the slope, K is the rate constant, and t is the isothermal dwell time. Although n is often linked to determining a possible diffusion mechanism for a sintering process, its origin was based on the experimental fitting upon which grain growth kinetics was developed. After determining n from varying the dwell time, Eq. (2) can be used to extrapolate average grain size at a given time where a small n value will estimate large grain size. Fig. 2b plots the empirical exponents from the reported ZnO grain size data [28,31]. It is evident that n value ranges widely different, which is sensitive to densification process variables including transient chemical reaction, sintering temperature, uniaxial pressure, and dwell time.

3.2. Specific surface area reduction kinetics

Considering the fundamental driving force for sintering, a particulate system is to reduce free energy by changing surface energy and surface area at the interfaces [32,33], which is denoted as:

$$\Delta G = A\Delta\gamma + \gamma\Delta A \tag{3}$$

where ΔG is the Gibb's free energy, A is the interface area, and γ is the interface energy. Here, the area of solid–vapor interface can be quantified by physisorption of gas molecules or mercury intrusion [34,35]. For sintering studies, the specific surface area measurement can provide comprehensive information to evaluate sintering kinetics as such technique is sensitive to the effects of mass transport mechanisms [17,36,37]. Fig. 3a–d illustrates the changes in particle surface area during a sintering process. Comparing the cases of Fig. 3a and b, the specific surface area is not changed by particle compaction under uniaxial pressure. In other words, packing without plastic deformation does not change the particle size and shape as to be expected with ceramic materials, unless there is brittle fracture, which was not observed in this study. In Fig. 3c, some degree of neck formation can occur at the beginning of isothermal dwell, leading to the reduction of the specific surface area. Fig. 3d highlights further decrease in solid–vapor interface during the isothermal dwell due to densification and pore elimination. Table 1 experimentally supports such notions by measuring the various conditions of ZnO specific surface area using the

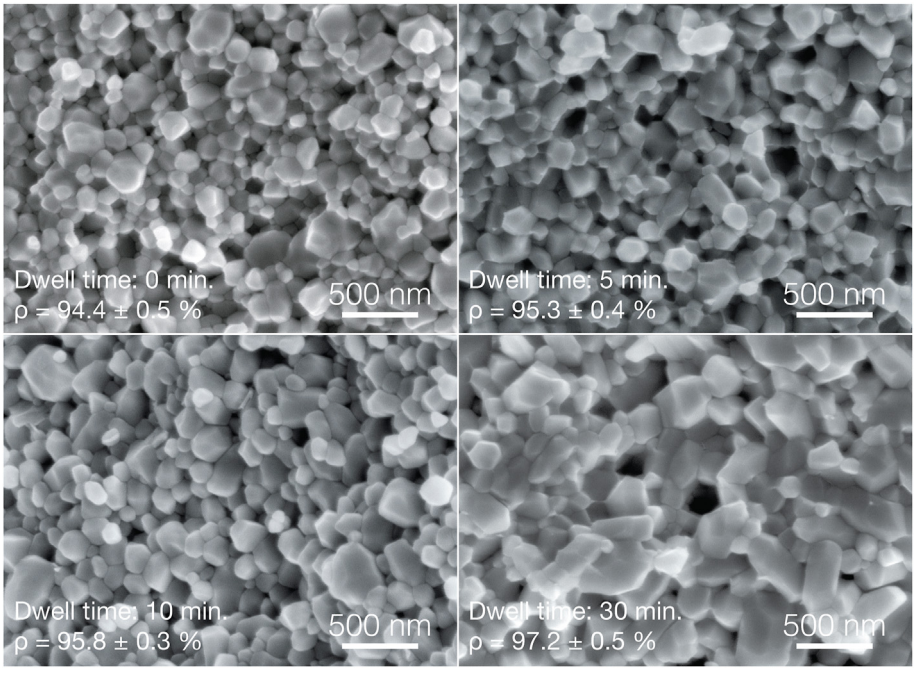

Fig. 1. Microstructure evolution of the fracture surfaces and relative density (ρ) after 0, 5, 10, and 30 minutes of isothermal dwell at 150 °C.

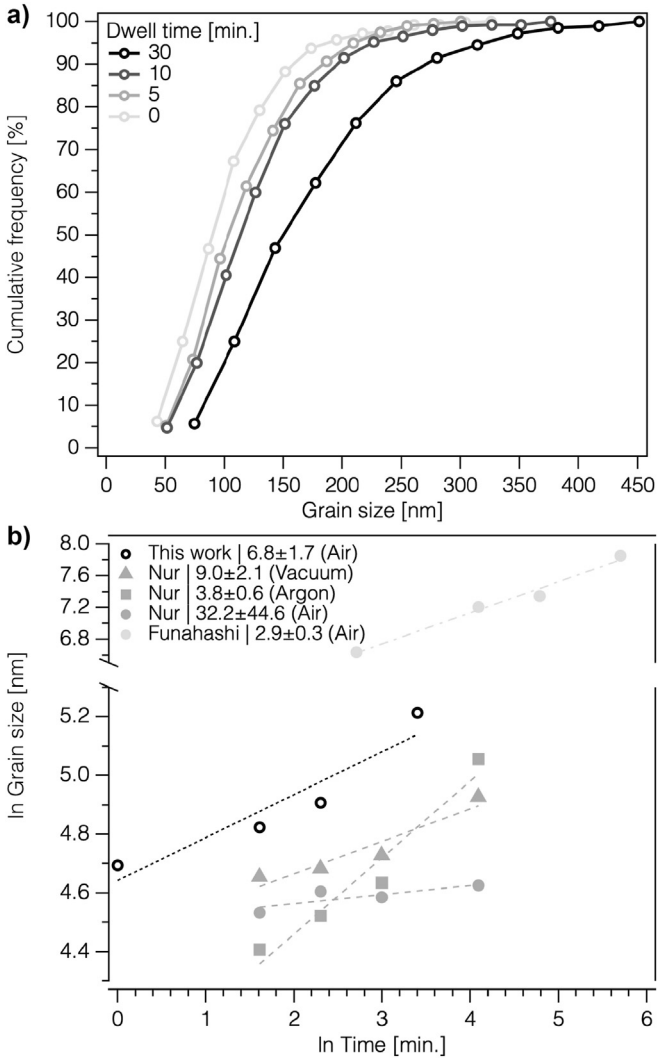

Fig. 2. (a) Cumulative frequency plot of grain size after 0, 5, 10, and 30 minutes of isothermal dwell at 150 °C where 400 grains were counted. (b) Determination and comparison of empirical exponent from average grain size and isothermal dwell time.

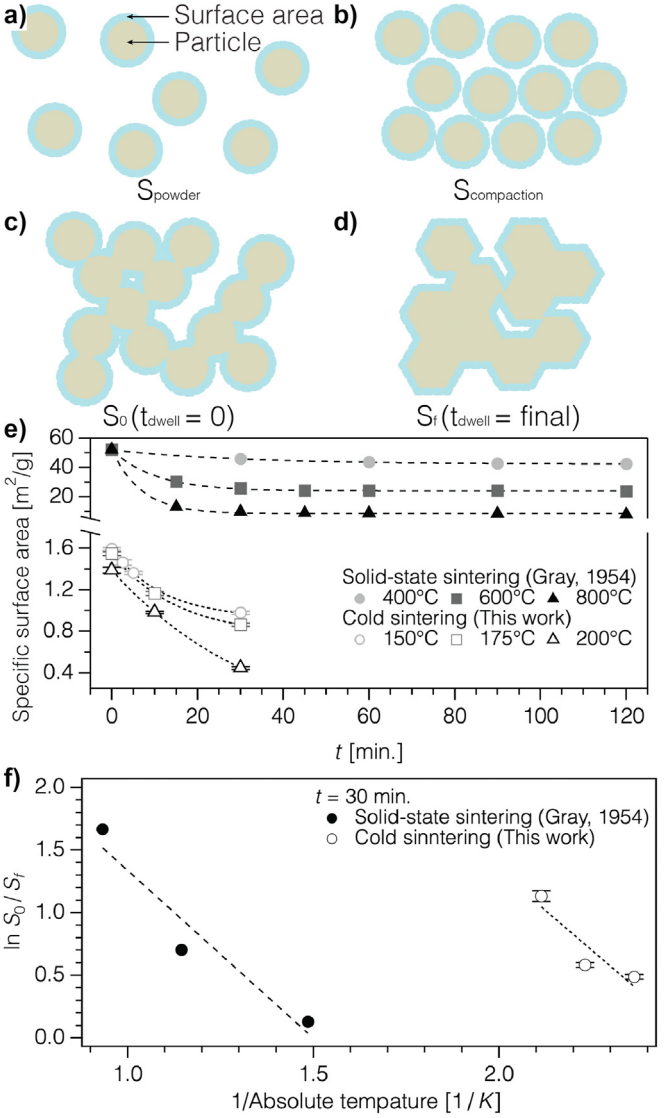

Fig. 3. Diagrams of specific surface area: a) powder, b) powder compaction, c) sintered for t_0, and d) sintered for t_f. e) ZnO specific surface area reduction a during dwell time. f) Arrhenius relation between the ratio of specific surface areas and inverse of sintering temperature.

Brunauer, Emmett, and Teller (BET) technique. In the case of cold sintering, It is clearly shown that pressing powder under 340 MPa does not change the specific surface area but noticeable reduction occurs during heating and isothermal dwell. The reported values [38,39] also demonstrate that systematic specific surface area reduction does depend on sintering temperature and time.

Hence, phenomenological equations have been progressively proposed to understand activation energetics for surface area reduction of particles [40–43]. In this study, the Schlaffer model is used to analyze the specific surface area data. This model has considerable merit in accurately fitting specific surface area changes across many sintering systems during the course of all stages ranges from initial to final [44]. The modified Schlaffer model is expressed as follows:

$$-\frac{dS}{dt} = kS^{-n} \tag{4}$$

where S is the specific surface area, t is time, k is the reaction rate constant depending on temperature, and n is the order of the reaction. Solving the given first-order nonlinear ordinary differential equation using separation of variables and imposing the physical conditions where the specific surface area is non-zero positive values, Eq. (4) now becomes:

$$\frac{S_0^{n+1} - S_f^{n+1}}{n+1} = k\left(t_f - t_0\right) \tag{5}$$

Note that t_0 is zero by the definition of the beginning of isothermal dwell. Then, Eq. (5) can be further simplified into:

$$\ln\left(\frac{S_0}{S_f}\right) = \left(\frac{1}{n+1}\right)\ln\left(kt_f(n+1)\right) \tag{6}$$

According to Eq. (6), n can be determined by experimental fitting over isothermal dwell data without the need of assuming the values of exponents based on a single diffusion mechanism. Then, the activation energy of surface area reduction is deduced from k where the reaction rate constant expressed in the form of Arrhenius equation:

Table 1
ZnO BET specific surface area (SSA) measurements of various conditions.

Sample	Condition	SSA [$m^2\ g^{-1}$]
S_{powder}	As-is	13.6±0.02
$S_{compaction}$	Uniaxial pressing under 340 MPa	13.6±0.01
S_0	At 0 minute of isothermal dwell at 150–200 °C	1.6–1.4
S_f	After 30 minutes of isothermal dwell at 150–200 °C	1.0–0.4
S_0 [38]	At 0 minute of isothermal dwell at 400–1000 °C	4.9–0.5
S_{powder} [39]	As-synthesized	52.0
S_f [39]	After 60 minutes of isothermal dwell at 400–800 °C	43.8–8.7

$$k = k_0 \exp\left(\frac{-E_a}{RT}\right) \tag{7}$$

Fig. S2 plots Eq. (6) for various n from negative to positive value and the arrow indicates its magnitude increases, showing how the ratio of S_0 to S_f changes over time. Considering the physical nature of S_0 and S_f where both values are positive and surface area only decreases over the time, n is logically deduced to be a positive parameter as the ratio will only increase over the time. Fig. 3e compares ZnO specific surface area as a function of isothermal dwell time between cold sintering process and solid-state sintering. In the case of cold sintering, it is evident that higher isothermal temperature results in a smaller S_0 and a faster reduction rate. However, in the case of reference solid-state sintering data [39], no clear distinction was made between S_{powder} and S_0, which may relate to the low sintering temperature used in the study where minimal neck formation was expected during the heating process. Other than the aforementioned difference, the solid-state sintering also shows a faster reduction rate at a higher isothermal temperature. Both of data sets comprehensively highlight the systematic evolution among specific surface area, sintering temperatures, and isothermal dwell times. Fig. 3f shows the Arrhenius relation between the ratio of specific surface area and inverse of sintering temperature after 30 minutes of isothermal dwell where the resulting linear fitting slope is differed by 5%. Table 2 summarizes the activation energy calculation based on the modified Schlaffer model shown in Eq. (6). The order of reaction, n, was experimentally determined for each sintering temperature where the resulting averages are 2.7±2.3 for the cold sintering process and 9.4±6.6 for solid-state sintering. Considering the implication of n parameter, this verifies that the reduction rate of surface area is significantly faster for the cold sintering process. The resulting values for the activation energy show that ZnO cold sintering requires only 33% of energetics of solid-state sintering to reduce solid-vapor interfaces and such a notable difference likely pertains to fast evolution of transient chemical interface rather than solid-state diffusion.

Table 2
Activation energy for ZnO specific surface area reduction of cold sintering process (CSP) and solid–state sintering (SS) [39] based on the modified Schlaffer model. n is the order of reaction at sintering temperature, n is the average of n, and E_a is the activation energy.

Method	Temperature [°C]	n	$\bar{n}$	E_a [kJ mol^{-1}]
CSP	150	4.9		
(this study)	175	2.7	2.7±2.3	77.4±68.3
	200	0.40		
SS	400	16.5		
(Gray, 1954)	600	8.3	9.4±6.6	231.3±169.5
	800	3.4		

However, the limitation of the analysis is that the distinction between S_0 and S_{powder} is not clear, which changes the ratio of specific surface area in Eq. (6). Such distinction is critical to understand the specific surface area reduction during the isothermal stage and to accurately apply the physical model. A significant experimental uncertainty of the cold sintering can be associated with the accelerated decomposition of anhydrous zinc acetate between 150 and 200 °C [45], which can be expressed by the following reaction:

$$Zn(CH_3COO)_2(s) + H_2O \rightarrow ZnO + 2CH_3COOH \tag{R1}$$

Therefore, the formation of ZnO is kinetically favored at a higher sintering temperature, which can influence the rate of specific surface area reduction. Indeed, it is clear that the experimentally determined n is highly sensitive to sintering temperatures for both sintering techniques, leading to a considerable uncertainty to activation energy calculation. However, it is correctly reflecting the specific surface area reduction behaviors with respect to sintering time and temperature [46] Such analysis can be considered as a preliminary investigation to understand the transition from the solid–vapor interface to the solid–solid interface during the cold sintering process, which can be compared to that of solid-state sintering. Moreover, the cold sintering process can, for example, offer unique processing opportunities for fabricating solid-state battery composite materials [47–49] where understanding the evolution of specific surface is crucial to control performance characteristics such as impedance, capacity, and charging and discharging rates [50].

3.3. Chemical evolution

As the major driving force for the cold sintering process is a chemical reaction between host powder and transient liquid phase, it is crucial to understand chemical evolution during the sintering process where the FTIR technique has been increasingly used for studying local chemical environment [20]. Fig. 4a shows IR spectra of the starting ZnO powder, acetic acid solution, and reference zinc acetate dihydrate powder for accounting the formation of zinc acetate complexes [21,51]. Fig. 4b presents IR spectra at the different stages of cold sintering from mixing to isothermal dwell up to 120 minutes and Table S1 summarizes possible corresponding molecular vibrations for observed wavenumbers. For the starting ZnO powder, the observed bands at 3450, 1648, and 1288 cm^{-1} indicate humidity absorption, which is in agreement with the previously reported TGA data [21]. When the zinc oxide powder and 2 M acetic acid solution are mixed at room temperature, new bands around 1630 and 1393 cm^{-1} likely suggest the formation of zinc carboxylate complex. In order to estimate the coordination type of the complex, it is reported that the difference in the wavenumbers of symmetrical and antisymmetrical vibration modes of the carboxyl groups ($\Delta\nu_{a-s} = \nu_a(COO^-) - \nu_s(COO^-)$) can be used to determine the bonding force of acetate anion and zinc cations [52]. However, the mixture does not present the corresponding absorbance around 1445 cm^{-1} for the symmetrical vibration mode, so further investigation is needed to fully understand the detailed coordination of the carboxylate ligands. During the heating to 200 °C, the major bands at 1547 and 1393 cm^{-1} gradually attenuate and no organic group is detectable after 120 minutes of isothermal dwell. The given spectroscopic study provides concrete experimental observations about the chemical evolution of the transient phases during the ZnO cold sintering process. Once zinc carboxylate complex forms by mixing ZnO and acetic acid solution, it is presented in the system and involved in densification and grain growth. Like the name,

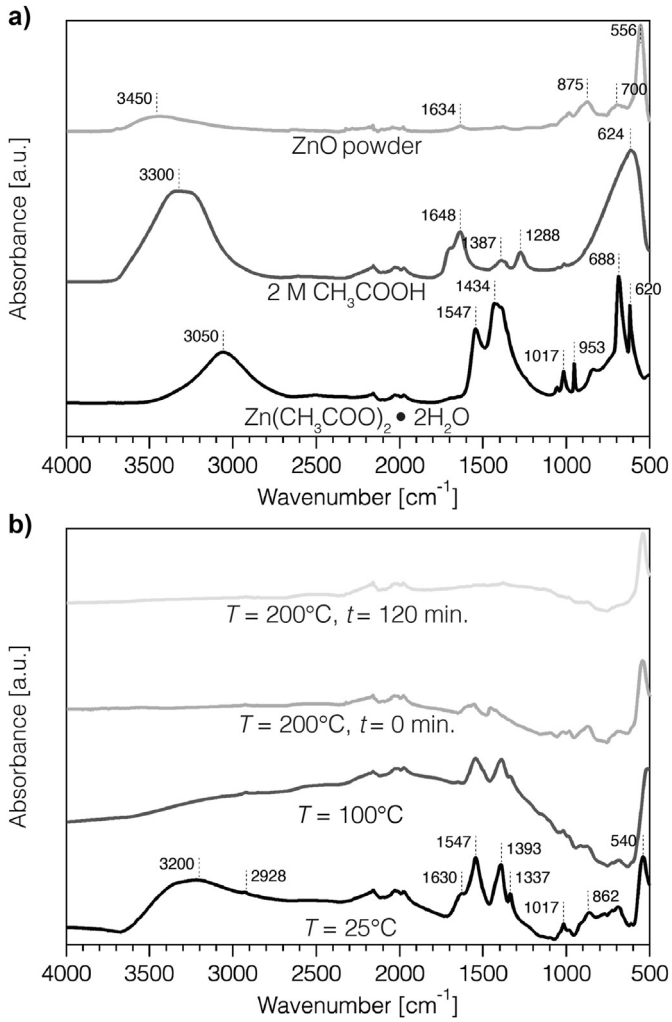

Fig. 4. FTIR analysis. a) Reference zinc acetate dihydrate powder (Sigma-Aldrich ACS reagent, ≥ 98%), 2 M acetic acid solution, and zinc oxide powder. b) Mixture of zinc oxide powder and 2 M acetic acid solution, cold-sintering quenched at 100 °C, quenched at 200 °C, isothermal dwell for 120 minutes at 200 °C.

"transient" implies, controlled isothermal dwell can result in residual-free ZnO polycrystalline ceramic.

3.4. Morphological evolution of transient interface

In order to further understand the ZnO morphological and chemical evolution during isothermal dwell, TEM and EDS measurements were carried out. In the case of a 0-minute isothermal dwell sample, Fig. 5a shows a low-magnification image capturing overall dense microstructure with small population of bright spots, possibly pertaining to mass or thickness contrast. Fig. 5b reveals the interface between ZnO grain and the bright spot in high-magnification, evidently displaying the recrystallization near the interface while the presence of amorphous phase further away from the interface. Fig. 5c characterizes the elemental composition of the associated area, verifying that the bright spot is composed of carbon, which is due to the formation of zinc acetate complex. Moreover, the line profile shows that carbon seems to segregate at the interfaces, implying that molecular dynamics may be distinctively different between crystalline ZnO grain and amorphous zinc acetate complex. After 30 minutes of isothermal dwell, however, such a transient interface is now significantly changed. Fig. 5d presents a low-magnification micrograph of dense microstructure with a frequent population of large grains and reduced bright spots. Fig. 5e captures the triple point of ZnO grains in high-magnification where the small center area does not show obvious lattice fringe, suggesting the presence of the amorphous phase. Also, the grain-to-grain interface is clean due to complete recrystallization. Fig. 5f verifies that the center area is filled with carbon and the smaller size compared to the 0-minute case indicates that the transient chemical reaction is now very close to the completion. The presented TEM data brings important discoveries regarding the existence and evolution of the transient phases at the interface during isothermal dwell. Moreover, controlling the amorphous and residual phase on these grain boundaries is a critical determinant to electrical and mechanical properties of a cold-sintered ZnO sample [31,53].

Based on the experimental interface characterization, the following schematic is proposed to conceptualize morphological changes occurring at the transient interface. Fig. 5g illustrates the formation of the transient phase on the grain surface by the chemical reaction between ZnO powder and acetic acid solution. Under isothermal dwell and uniaxial pressure, Fig. 5h highlights the recrystallization of the transient phases onto the existing crystalline grains through Ostwald ripening process and decomposition of organic species. Fig. 5i displays the pore closure as a result of continuous recrystallization until the depletion of the transient phase. The given idea has a close similarity to the concept of grain-scale dynamic recrystallization used in earth science. Also known as syntectonic recrystallization, dynamic recrystallization is synchronous with deformation where materials from the grain are formed in the grain boundary region and consumed for the recrystallization on the lattice of an adjacent grain that is going under grain growth [54]. Considering the use of low-temperature, deviatoric stress, and fluid-enhanced chemical activities, we find that profound analogies can be made between the cold sintering process and geological deformation process, which can bring new insight to understand low-energy densification.

3.5. ReaxFF simulation

The experimental analysis shows that there is an increased carbon content in the grain boundary region of the cold-sintered pellet. In order to understand the interfacial dynamics in this corresponding region, we modeled the ZnO–solvent interface by conducting molecular dynamics simulations using ReaxFF interatomic potential [55]. The ZnO surface modeled in this study is the ZnO $(10\bar{1}0)$ plane, and the solvent is a mixture of Zn^{2+} ions, acetic acid and water molecules. To model such chemical systems using ReaxFF, force fields are prepared to reproduce the reference chemical events obtained by quantum chemical methods, such as density functional theory, using ReaxFF dynamics simulations method. Then the force field can be applied to larger molecular systems for longer simulation times. The ReaxFF force field used in this study has been successfully applied to model surface reaction kinetics in cold sintering process [23,25,56]. Fig. 6a displays the initial configuration of the simulation which was prepared by homogeneously distributing the Zn^{2+} ions, acetic acid and water molecules to create a solve phase. The temperature was increased to 600 K to simulate the evaporation stage of cold sintering inside pore region at the ZnO–solvent interface. Please refer to the computational method section for more details.

According to the simulation, with the increase of temperature, outer hydration shells around Zn^{2+} ions in the solve phase are dissociated. The removal of water molecules around the ions reduces the permittivity of the medium, and thus, enhances the

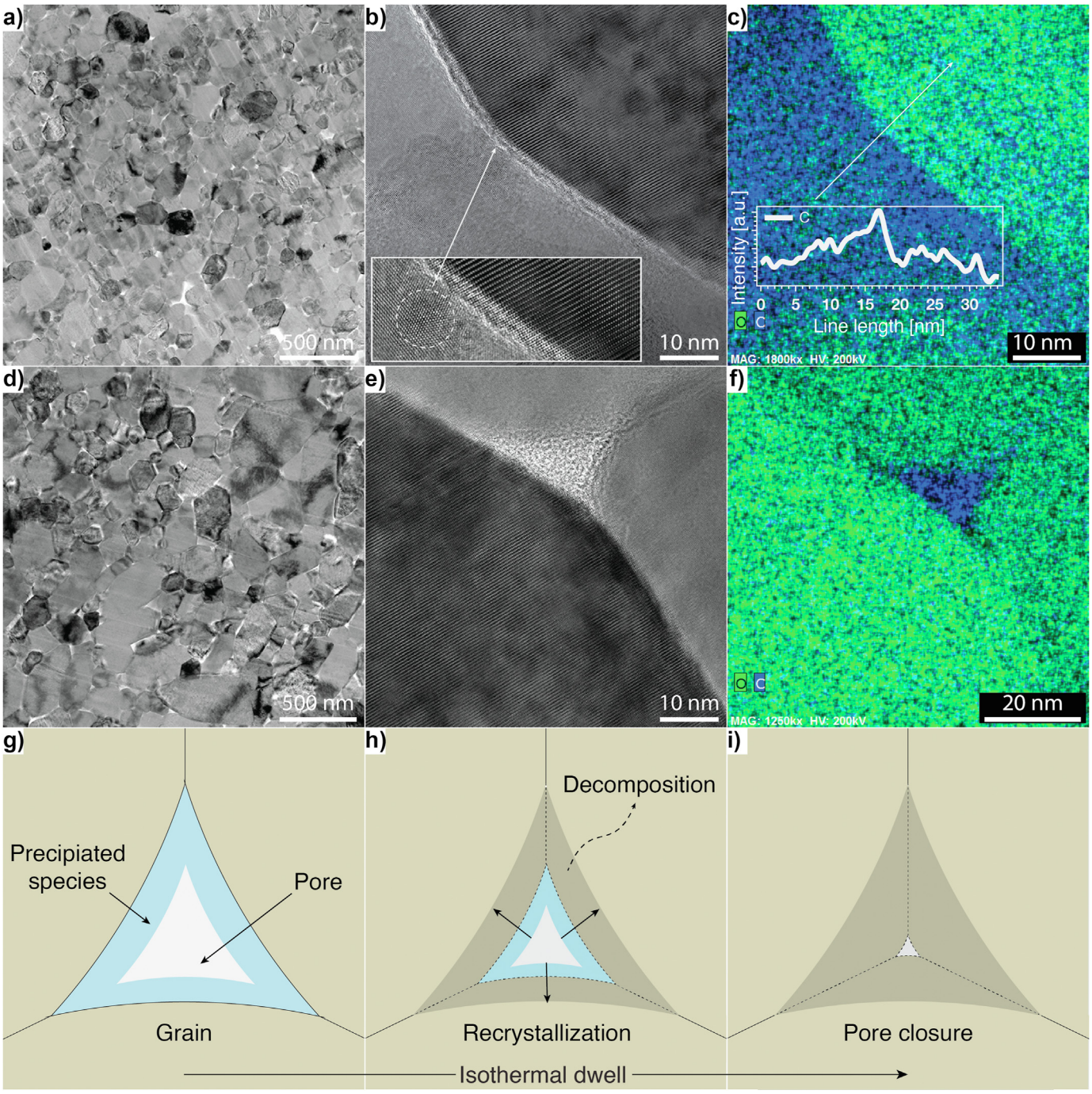

Fig. 5. Microstructure after 0-minute isothermal dwell: (a) low-magnification of bright field image, (b) high-magnification where the inset graph displays the recrystallization near the interface, and (c) EDS mapping highlighting the carbon-rich phase at interface; Microstructure after 30-minute isothermal dwell: (d) low-magnification, (e) high-magnification, and (f) EDS mapping. Proposed schematics for recrystallization and pore closure at the interface. (g) precipitation occurs at the pore, (h) surface recrystallization onto a neighboring grain and decomposition of organic species, and (i) pore closure.

interatomic interactions. Our simulations demonstrate that water molecules around Zn^{2+} ions in the solvent phases are dissociated at the early stages of temperature increase, and acetic acid (or acetate) molecules tend to substitute these water molecules based on the following chemical reaction:

$$Zn{\cdot}4H_2O + 2CH_3COOH \rightarrow Zn(CH_3COOH)_2{\cdot}nH_2O + (4n)H_2O \quad (R2)$$

The binding of acetic acid is observed monodentate; however, may switch to bidentate form with the increase of temperature due to the desorption of water and/or deprotonation of acetic acid. The binding between Zn^{2+} and acetic acid is stronger than that of Zn^{2+} and water [23]; therefore, we observe in the simulations that when the system is reached to equilibration, the density of organic molecules is higher around the ions. The temperature increase does not only dissociate the hydration shells around ions in the solution phase, but it also removes the tightly bound structured water layer on the oxide surface, which enhances the precipitation of ions from the solvent phase to the surface. As a result, Zn^{2+} ions tend to precipitate before organic acids are removed from the system and

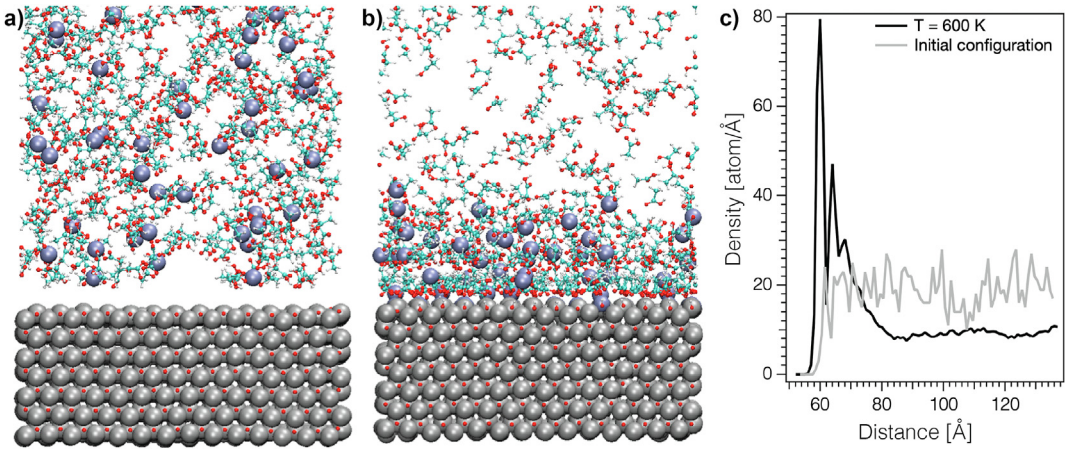

Fig. 6. The influence of temperature to the carbon distribution at the ZnO−water−acetic acid interface. (a) The initial configuration of the simulation box, which shows the state before the temperature is increased. It shows that the carbon density is homogeneously distributed through the direction perpendicular to the ZnO surface. (b) The final configuration of the simulation box, which shows the state after the temperature is increased and the simulation box is equilibrated at that temperature. It shows the carbon-rich layer on the surface. Key: Zn^{2+} ion in solvent phase (purple), oxygen atom (red), hydrogen atom (white), carbon atom (cyan), zinc atom in condensed phase (gray). Only one side of the surface is given, and water molecules are hidden in visualization to increase the visibility of carbon−rich region. c) The density of carbon atoms with respect to the distance from the ZnO surface, indicating a strong binding of the zinc acetate complex to the ZnO surface.

thus carry these adsorbed molecules. As a result of the precipitation, Fig. 6b shows a stable carbon-rich layer is created on the surface. Fig. 6c consequently presents the increases of the carbon-content near the surface. The structure of the stable layer is mostly composed of zinc acetates where acetate molecules act as a bridging complex to connect Zn^{2+} ions to another one or the surface. The timescales in this simulation are limited to observe crystallization of zinc−acetate epitaxial layers; however, it is safe to assume that the precipitated carbon-rich layer initiates the carbon-rich crystal regions as seen in the TEM images because the temperatures used in cold sintering is too low to dissociate this layer. Using increased temperatures may trigger the decomposition of acetate in the system and avoid zinc acetate formation.

4. Conclusions

As the technological and environmental values of the cold sintering process have been highlighted among diverse scientific communities for various applications, thorough understanding of its underlying mechanisms is needed to be addressed. Taking ZnO as a model sintering system, this study focuses on investigating the morphological and chemical evolution of transient interfaces during isothermal dwell. Gas physisorption measures that specific surface area is gradually reduced between 0 and 30 minutes, indicating the decrease in solid-vapor interfaces due to grain growth. Moreover, according to the Schlaffer model, the activation energy for specific surface area reduction was 77 kJ/mol whereas solid-state sintering was 231 kJ/mol, suggesting the rapid pore closure under the cold sintering conditions. Infrared spectroscopy finds the formation of zinc carboxylate complex after mixing the host ZnO powder and acetic acid solution, and the new bands around 1547 and 1393 cm^{-1}, were continuously appeared during heating. However, neither carboxyl nor hydroxyl group was detected after isothermal dwell, showing an organic residual-free ZnO phase. High-resolution micrographs capture the recrystallization occuring between crystalline grain and amorphous carbon-rich phase where carbon was segregated at the interface. During the 30 minutes of isothermal dwell, the grain growth was observed while the amorphous phase was evidently shrunk, reasonably proposing that zinc carboxylate complex may be consumed for the recrystallization on the lattice of a neighboring grain. ReaxFF molecular dynamics simulation provide in-depth information about chemical activities at the interface, revealing the formation of zinc acetate complex and the precipitation of carbon-rich layer on the ZnO surface. Considering the comprehensive and coherent experimental validations in conjunction with the simulations, this study contributes to the deep understanding of the transient evolution during the cold sintering process.

CRediT author statement

Sun Hwi Bang: Investigation, Visualization, Writing − original draft. Mert Y. Sengul: Methodology, Software, Validation. Zhongming Fan: Investigation. Arnaud Ndayishimiye: Writing − review and editing. Adri C. T. van Duin: Funding acquisition, Supervision. Clive A. Randall: Funding acquisition, Supervision.

Declaration of competing interest

The authors declare that they have no known competing financial interests or personal relationships that could have appeared to influence the work reported in this paper.

Acknowledgements

The authors thank National Science Foundation for supporting fundamental cold sintering mechanism study (DMR-1728634) and for enabling interfacial dynamics simulation using ReaxFF interatomic potential (DMR-1842922). Also, the authors greatly appreciate research staff in the Materials Characterization Laboratory of Penn State Materials Research Institute.

Appendix A. Supplementary data

Supplementary data to this article can be found online at https://doi.org/10.1016/j.mtchem.2022.100925.

References

[1] D.W. Richerson, Modern Ceramic Engineering: Properties, Processing, and Use in Design, CRC Press, 2005.
[2] A.G. Bloxam, Improved manufacture of electric incandescence lamp filaments from tungsten or molybdenum or an alloy thereof, British Patent 27 (1906), 002.

[3] O. Guillon, J. Gonzalez-Julian, B. Dargatz, T. Kessel, G. Schierning, J. Räthel, M. Herrmann, Field-assisted sintering technology/spark plasma sintering: mechanisms, materials, and technology developments, Adv. Eng. Mater. 16 (7) (2014) 830–849.
[4] J.C. Mankins, Technology readiness levels, White Paper, April 6 (1995).
[5] G. Kuczynski, Towards the understanding of the process of sintering, in: Sintering'85, Springer, 1987, pp. 3–16.
[6] H. Su, D.L. Johnson, Master sintering curve: a practical approach to sintering, J. Am. Ceram. Soc. 79 (12) (1996) 3211–3217.
[7] T. Kutty, K. Khan, P. Hegde, J. Banerjee, A. Sengupta, S. Majumdar, H. Kamath, Development of a master sintering curve for tho2, J. Nucl. Mater. 327 (2–3) (2004) 211–219.
[8] D.C. Blaine, J.D. Gurosik, S.J. Park, R.M. German, D.F. Heaney, Master sintering curve concepts as applied to the sintering of molybdenum, Metall. Mater. Trans. 37 (3) (2006) 715–720.
[9] O. Guillon, J. Langer, Master sintering curve applied to the field-assisted sintering technique, J. Mater. Sci. 45 (19) (2010) 5191–5195.
[10] T. Frueh, I. Ozer, S. Poterala, H. Lee, E.R. Kupp, C. Compson, J. Atria, G.L. Messing, A critique of master sintering curve analysis, J. Eur. Ceram. Soc. 38 (4) (2018) 1030–1037.
[11] T. Ibn-Mohammed, C.A. Randall, K. Mustapha, J. Guo, J. Walker, S. Berbano, S. Koh, D. Wang, D. Sinclair, I. Reaney, Decarbonising ceramic manufacturing: a techno-economic analysis of energy efficient sintering technologies in the functional materials sector, J. Eur. Ceram. Soc. 39 (16) (2019) 5213–5235.
[12] C.A. Randall, J. Guo, A. Baker, M. Lanagan, G. Hanzheng, Cold Sintering Ceramics and Composites, US Patent App, Mar. 30 2017, p. 553, 15/277.
[13] T.H. de Beauvoir, S. Dursun, L. Gao, C. Randall, New opportunities in metallization integration in cofired electroceramic multilayers by the cold sintering process, ACS Applied Electronic Materials 1 (7) (2019) 1198–1207.
[14] D. Wang, S. Zhang, G. Wang, Y. Vardaxoglou, W. Whittow, D. Cadman, D. Zhou, K. Song, I.M. Reaney, Cold sintered catio3-k2moo4 microwave dielectric ceramics for integrated microstrip patch antennas, Appl. Mater. Today 18 (2020) 100519.
[15] Z. Grady, Z. Fan, A. Ndayishimiye, C.A. Randall, Design and sintering of all-solid-state composite cathodes with tunable mixed conduction properties via the cold sintering process, ACS Appl. Mater. Interfaces 13 (40) (2021) 48071–48087.
[16] J. Mackenzie, R. Shuttleworth, A phenomenological theory of sintering, Proc. Phys. Soc. B 62 (12) (1949) 833.
[17] R.M. German, Sintering trajectories: description on how density, surface area, and grain size change, J. Miner. Met. Mater. Soc. 68 (3) (2016) 878–884.
[18] K. Tsuji, A. Ndayishimiye, S. Lowum, R. Floyd, K. Wang, M. Wetherington, J.-P. Maria, C.A. Randall, Single step densification of high permittivity batio3 ceramics at 300^{o}c, J. Eur. Ceram. Soc. 40 (4) (2020) 1280–1284.
[19] K. Tsuji, T. Herisson de Beauvoir, A. Ndayishimiye, K. Wang, C.A. Randall, Cold sintering of yttria-stabilized cubic bismuth oxide: conductivity and microstructural evolution of metastable grain boundaries with annealing, J. Appl. Phys. 128 (21) (2020) 215104.
[20] K. Rubenis, S. Zemjane, J. Vecstaudza, J. Bitenieks, J. Locs, Densification of amorphous calcium phosphate using principles of the cold sintering process, J. Eur. Ceram. Soc. 41 (1) (2021) 912–919.
[21] S.H. Bang, A. Ndayishimiye, C.A. Randall, Anisothermal densification kinetics of the cold sintering process below 150°C, J. Mater. Chem. C 8 (17) (2020) 5668–5672.
[22] E. Cauët, S. Bogatko, J.H. Weare, J.L. Fulton, G.K. Schenter, E.J. Bylaska, Structure and dynamics of the hydration shells of the zn 2+ ion from ab initio molecular dynamics and combined ab initio and classical molecular dynamics simulations, J. Chem. Phys. 132 (19) (2010) 194502.
[23] M.Y. Sengul, C.A. Randall, A.C. van Duin, Reaxff molecular dynamics study on the influence of temperature on adsorption, desorption, and decomposition at the acetic acid/water/zno (1010) interface enabling cold sintering, ACS Appl. Mater. Interfaces 10 (43) (2018) 37717–37724.
[24] M.Y. Sengul, C.A. Randall, A.C. van Duin, Reaxff molecular dynamics simulation of intermolecular structure formation in acetic acid-water mixtures at elevated temperatures and pressures, J. Chem. Phys. 148 (16) (2018) 164506.
[25] M.Y. Sengul, J. Guo, C.A. Randall, A.C. van Duin, Water-mediated surface diffusion mechanism enables the cold sintering process: a combined computational and experimental study, Angew. Chem. 131 (36) (2019) 12550–12554.
[26] E.J. Baerends, T. Ziegler, A. Atkins, J. Autschbach, D. Bashford, A. Bérces, F. Bickelhaupt, C. Bo, P.M. Boerritger, L. Cavallo, C. Daul, D.P. Chong, D.V. Chulhai, D.V. Chulhai, L. Deng, R.M. Dickson, J.M. Dieterich, D.E. Ellis, M. van Faassen, A. Ghysels, A. Giammona, S.J.A. van Gisbergen, A. Goez, A.W. Gtz, S. Gusarov, F.E. Harris, P. van den Hoek, Z. Hu, C.R. Jacob, H. Jacobsen, L. Jensen, L. Joubert, J.W. Kaminski, G. van Kessel, C. Knig, F. Kootstra, A. Kovalenko, M. Krykunov, E. van Lenthe, D.A. McCormack, A. Michalak, M. Mitoraj, S.M. Morton, J. Neugebauer, V.P. Nicu, L. Noodleman, V.P. Osinga, S. Patchkovskii, M. Pavanello, C.A. Peeples, P.H.T. Philipsen, D. Post, C.C. Pye, H. Ramanantoanina, P. Ramos, W. Ravenek, J.I. Rodrguez, P. Ros, R. Rger, P.R.T. Schipper, D. Schlns, H. van Schoot, G. Schreckenbach, J.S. Seldenthuis, M. Seth, J.G. Snijders, ADF2017, SCM, Theoretical Chemistry, Vrije Universiteit, Amsterdam, The Netherlands, 2017. URL, https://www.scm.com/.
[27] H.J. Berendsen, J.v. Postma, W.F. van Gunsteren, A. DiNola, J.R. Haak, Molecular dynamics with coupling to an external bath, J. Chem. Phys. 81 (8) (1984) 3684–3690.
[28] K. Nur, T.P. Mishra, J.G.P. da Silva, J. Gonzalez-Julian, M. Bram, O. Guillon, Influence of powder characteristics on cold sintering of nano-sized zno with density above 99%, J. Eur. Ceram. Soc. 41 (4) (2021) 2648–2662.
[29] S. H. Bang, C. A. Randall, Pressure-dependent topographic evolutions of cold-sintered zinc oxide surfaces, J. Mater. Chem. C doi:10.1039/D1TC04651A.
[30] Y. Iida, Sintering of high-purity nickel oxide, J. Am. Ceram. Soc. 41 (10) (1958) 397–406.
[31] S. Funahashi, J. Guo, H. Guo, K. Wang, A.L. Baker, K. Shiratsuyu, C.A. Randall, Demonstration of the cold sintering process study for the densification and grain growth of zno ceramics, J. Am. Ceram. Soc. 100 (2) (2017) 546–553.
[32] G.C. Kuczynski, Self-diffusion in sintering of metallic particles, Trans. AIME 185 (3) (1949) 169–178.
[33] W.D. Kingery, H.K. Bowen, D.R. Uhlmann, Introduction to Ceramics, vol. 17, John Wiley & Sons, 1976.
[34] E.-S. Jang, C.-W. Kang, Investigation of sound absorption properties of heat-treated Indonesian momala (homalium foetidum (roxb.) benth.) and Korean red toon (toona sinensis (a. juss.) m. roem.) cross sections, Forests 12 (11) (2021) 1447.
[35] O. Whittemore, J. Varela, Initial sintering of zno, J. Am. Ceram. Soc. 64 (11) (1981). C–154.
[36] H. Exner, G. Petzow, Shrinkage and rearrangement during sintering of glass spheres, in: Sintering and Catalysis, Springer, 1975, pp. 279–293.
[37] L.P. Martin, M. Rosen, Correlation between surface area reduction and ultrasonic velocity in sintered zinc oxide powders, J. Am. Ceram. Soc. 80 (4) (1997) 839–846.
[38] L. Perazolli, E. Longo, J.A. Varela, Sintering kinetics of zno during initial stage, in: Sintering Technology, Marcel Dekker, 1996, pp. 77–84.
[39] T. Gray, Sintering of zinc oxide, J. Am. Ceram. Soc. 37 (11) (1954) 534–538.
[40] W. Schlaffer, C. Morgan, J. Wilson, Aging of silica-alumina cracking catalyst. i. kinetics of structural changes by eeat and steam, J. Phys. Chem. 61 (6) (1957) 714–722.
[41] D. Nicholson, Variation of surface area during the thermal decomposition of solids, Trans. Faraday Soc. 61 (1965) 990–998.
[42] R. German, Z. Munir, Surface area reduction during isothermal sintering, J. Am. Ceram. Soc. 59 (9–10) (1976) 379–383.
[43] R. German, Surface area reduction kinetics during intermediate stage sintering, J. Am. Ceram. Soc. 61 (5–6) (1978) 272–274.
[44] S. Bailliez, A. Nzihou, The kinetics of surface area reduction during isothermal sintering of hydroxyapatite adsorbent, Chem. Eng. J. 98 (1–2) (2004) 141–152.
[45] A.V. Ghule, K. Ghule, C.-Y. Chen, W.-Y. Chen, S.-H. Tzing, H. Chang, Y.-C. Ling, In situ thermo-tof-sims study of thermal decomposition of zinc acetate dihydrate, J. Mass Spectrom. 39 (10) (2004) 1202–1208.
[46] D. Bregiroux, S. Lucas, E. Champion, F. Audubert, D. Bernache-Assollant, Sintering and microstructure of rare earth phosphate ceramics REPO4 with RE= La, Ce or Y, J. Eur. Ceram. Soc. 26 (3) (2006) 279–287.
[47] Z. Grady, A. Ndayishimiye, C. Randall, A dramatic reduction in the sintering temperature of the refractory sodium β-alumina solid electrolyte via cold sintering, J. Mater. Chem. 9 (38) (2021) 22002–22014.
[48] P. Jiang, P. Guo, Y. Shi, S. Li, K. Li, X. Lu, Z. Zhang, D. He, J. Bian, X. Lu, Solid-state Li metal battery enabled by cold sintering at 120°c, Materials Today Physics 20 (2021) 100476.
[49] X. Wang, J. Wang, F. Li, F. Zhu, C. Ma, Influence of cold sintering process on the structure and properties of garnet-type solid electrolytes, Ceram. Int. 46 (11) (2020) 18544–18550.
[50] Y. Xia, M. Yoshio, H. Noguchi, Improved electrochemical performance of lifepo4 by increasing its specific surface area, Electrochim. Acta 52 (1) (2006) 240–245.
[51] A. Ndayishimiye, M.Y. Sengul, S.H. Bang, K. Tsuji, K. Takashima, T.H. de Beauvoir, D. Denux, J.-M. Thibaud, A.C. van Duin, C. Elissalde, et al., Comparing hydrothermal sintering and cold sintering process: mechanisms, microstructure, kinetics and chemistry, J. Eur. Ceram. Soc. 40 (4) (2020) 1312–1324.
[52] Y. Wang, Y. Li, Z. Zhou, X. Zu, Y. Deng, Evolution of the zinc compound nanostructures in zinc acetate single-source solution, J. Nanoparticle Res. 13 (10) (2011) 5193.
[53] K. Nur, M. Zubair, J. S.-L. Gibson, S. Sandlöbes-Haut, J. Mayer, M. Bram, O. Guillon, Mechanical properties of cold sintered zno investigated by nano-indentation and micro-pillar testing, J. Eur. Ceram. Soc..
[54] J. Urai, W. Means, G. Lister, Dynamic recrystallization of minerals, in: Mineral and Rock Deformation: Laboratory Studies, vol. 36, AGU, Washington, DC, 1986, pp. 161–199.
[55] A.C. Van Duin, S. Dasgupta, F. Lorant, W.A. Goddard, Reaxff: a reactive force field for hydrocarbons, J. Phys. Chem. 105 (41) (2001) 9396–9409.
[56] A. Ndayishimiye, M.Y. Sengul, D. Akbarian, Z. Fan, K. Tsuji, S.H. Bang, A.C. Van Duin, C.A. Randall, Dynamics of the chemically driven densification of barium titanate using molten hydroxides, Nano Lett. 21 (8) (2021) 3451–3457.